SANDIA REPORT
SAND2008-6217
Unlimited Release
Printed September 2008

Mid-Infrared Quantum Dot Emitters Utilizing Planar Photonic Crystal Technology

Eric A. Shaner, Brandon Passmore, Sungkwun K. Lyo, Jeff Cederberg, Ganesh Subramania, Ihab El-Kady

Prepared by
Sandia National Laboratories
Albuquerque, New Mexico 87185 and Livermore, California 94550

Sandia is a multiprogram laboratory operated by Sandia Corporation,
a Lockheed Martin Company, for the United States Department of Energy's
National Nuclear Security Administration under Contract DE-AC04-94AL85000.

Approved for public release; further dissemination unlimited.

Sandia National Laboratories

Issued by Sandia National Laboratories, operated for the United States Department of Energy by Sandia Corporation.

NOTICE: This report was prepared as an account of work sponsored by an agency of the United States Government. Neither the United States Government, nor any agency thereof, nor any of their employees, nor any of their contractors, subcontractors, or their employees, make any warranty, express or implied, or assume any legal liability or responsibility for the accuracy, completeness, or usefulness of any information, apparatus, product, or process disclosed, or represent that its use would not infringe privately owned rights. Reference herein to any specific commercial product, process, or service by trade name, trademark, manufacturer, or otherwise, does not necessarily constitute or imply its endorsement, recommendation, or favoring by the United States Government, any agency thereof, or any of their contractors or subcontractors. The views and opinions expressed herein do not necessarily state or reflect those of the United States Government, any agency thereof, or any of their contractors.

Printed in the United States of America. This report has been reproduced directly from the best available copy.

Available to DOE and DOE contractors from
U.S. Department of Energy
Office of Scientific and Technical Information
P.O. Box 62
Oak Ridge, TN 37831

Telephone: (865) 576-8401
Facsimile: (865) 576-5728
E-Mail: reports@adonis.osti.gov
Online ordering: http://www.osti.gov/bridge

Available to the public from
U.S. Department of Commerce
National Technical Information Service
5285 Port Royal Rd.
Springfield, VA 22161

Telephone: (800) 553-6847
Facsimile: (703) 605-6900
E-Mail: orders@ntis.fedworld.gov
Online order: http://www.ntis.gov/help/ordermethods.asp?loc=7-4-0#online

SAND2008-6217
Unlimited Release
Printed September 2008

Mid-Infrared Quantum Dot Emitters Utilizing Planar Photonic Crystal Technology

Eric A. Shaner, Brandon Passmore and Sungkwun K. Lyo
Semiconductor Material & Device Sciences

Jeff Cederberg
Advanced Materials Sciences

Ganesh Subramania, and Ihab El-Kady
Photonic Microsystems Technology

Sandia National Laboratories
P.O. Box 5800
Albuquerque, New Mexico 87185-MS1415

Abstract

The three-dimensional confinement inherent in InAs self-assembled quantum dots (SAQDs) yields vastly different optical properties compared to one-dimensionally confined quantum well systems. Intersubband transitions in quantum dots can emit light normal to the growth surface, whereas transitions in quantum wells emit only parallel to the surface. This is a key difference that can be exploited to create a variety of quantum dot devices that have no quantum well analog. Two significant problems limit the utilization of the beneficial features of SAQDs as mid-infrared emitters. One is the lack of understanding concerning how to electrically inject carriers into electronic states that allow optical transitions to occur efficiently. Engineering of an injector stage leading into the dot can provide current injection into an upper dot state; however, to increase the likelihood of an optical transition, the lower dot states must be emptied faster than upper states are occupied. The second issue is that SAQDs have significant inhomogeneous broadening due to the random size distribution. While this may not be a problem in the long term, this issue can be circumvented by using planar photonic crystal or plasmonic approaches to provide wavelength selectivity or other useful functionality.

CONTENTS

1. Background 7
1.1. Motivation 7
1.2. InAs quantum dots 7

2. Accomplishments 8
2.1: InAs quantum dot material: theory 8
2.2: InAs quantum dot material: growth 9
2.3: InAs quantum dot material: characterization 10
2.4: Photonic crystal fabrication 11
2.5: Mid-IR plasmonics 12
2.5.1: Free-carrier tuning of plasmonic resonances 12
2.5.2: Temperature tuning of plasmonic resonances 15
2.5.3: Active Control of Propagating Surface Plasmons 18

3. Conclusions 22

4. References 23

Appendix A: Metrics 24

NOMENCLATURE

SAQD	Self Assembled Quantum Dot
Mid-IR	mid-infrared, 3 µm - 12 µm wavelength
QCL	Quantum Cascade Laser

1. BACKGROUND

1.1. Motivation

For many years, InAs self-assembled quantum dots (SAQDs) have been noted to have desirable optical properties due to their atomic-like quantum states (attributed to three-dimensional electron confinement). Even though quantum cascade laser (QCL) technology in the mid-infrared wavelength (mid-IR, 3 μm - 12 μm wavelength) has progressed rapidly using quantum well material (one-dimensional confinement), to date, we have yet to see useful mid-IR light emitters utilizing SAQDs. The primary reason for this gap is the current lack of knowledge pertaining to engineering SAQD electronic states in a manner analogous to that employed in QCLs. For SAQDs to be used in a similar fashion, we believe a new approach is necessary. One cannot simply insert a layer of SAQDs in an active region stage of a QCL and hope to get similar performance. We pursue engineering the materials surrounding the SAQDs to achieve desired electronic properties and to better understand the relevant SAQD physics. The key desired electronic properties are: 1) direct injection of electrons into an upper SAQD state that has an optical MIR transition to a lower state, 2) the electrons in the lower SAQD state need to be removed at a faster rate than those electrons in the upper SAQD state. Photonic crystal cavities and surface plasmon couplers integrated into SAQD material can provide a path towards wavelength selection, enhanced emission, and single photon mid-IR sources that may be useful for quantum communications. These platforms are both scientifically interesting, especially in the mid-IR, as well as being fundamentally important building blocks in mid-IR photonics.

1.2. InAs quantum dots

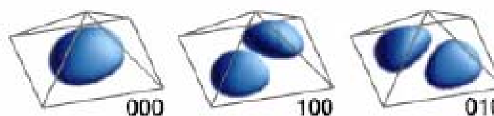

Fig. 1.1: Pyramid model of InAs SAQDs embedded in GaAs. Shown are the calculated ground state (000) and first excited state (100, 010) spatial electron wavefunction probabilities. As shown, electrons in the ground state are confined more to the center of the SAQD while excited state electrons spend more time near the edges. Image taken from Ref. 1.

InAs SAQDs form as three-dimensional lens or pyramidal shaped islands on GaAs, AlGaAs, or AlAs. Figure 1.1 shows the widely accepted electron wavefunction probabilities for InAs SAQDs embedded in GaAs[1]. The blue areas shown represent the probable location for an electron to be found in space for a given energy level. The electron ground state (000) is strongly confined to the center of the SAQD while the upper (100) and (010) electron states have a higher probability of being confined at the corners of the SAQD. These quantum dot states make up the primary optical transition in our mid-IR material. Their relative spacing and position with respect to the GaAs conduction band edge can be controlled through growth conditions that alter the size and density of the SAQDs, and also by growing the SAQDs on different materials, such as AlAs.

2. ACCOMPLISHMENTS

2.1: InAs quantum dot material: theory

One of the major obstacles for working with InAs quantum dots in tunneling structures is the lack of a mature theoretical framework, such as that behind QCL technology. The key difference here is that, rather than considering tunneling between quantum wells (2D-2D), one has to consider tunneling between quantum dots and wells (0D-2D).

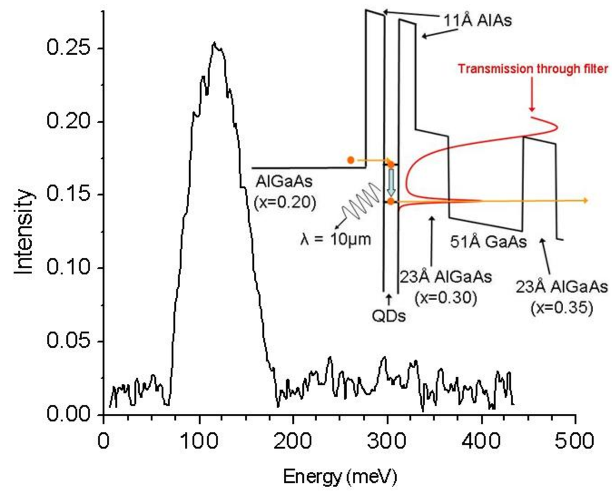

Fig. 2.1: EL spectrum from a surface-emitting MIR SAQD device. Inset shows the bandstructure of the device, under ~120meV bias. Electrons are injected into SAQD excited states from the AlGaAs/AlAs injector where electrons can transition to lower states by emitting a photon and then escape through the lower transmission band in the QW filter structure.

An example of an experimental 'guess' at a working structure is shown in Fig. 2.1. As shown in the inset, the device consists of an injector stage that feeds the upper quantum dot state, followed by a filtering collection stage to extract electrons from the lower dot state after emission of a mid-IR photon. This approach is quite similar to a single stage in a mid-IR QCL. While this guess worked to some extent, without getting into the transport theory of the problem, it was not known how to improve the material. The summary details of this transport theory are explained in the remainder of this section.

In the model structure Fig. 2.2, under a sufficiently large bias, the p-level of the InAs QD lies between the bottom of the conduction band E_c and the Fermi level E_F of the electron gas of the wide QW on the left side in contact with the source. The electrons tunnel into the p-state of the QD, fall down to the s-state emitting light, and tunnel out into the GaAs QW in contact with the drain. Important parameters that enter the theoretical formalism are the forward/backward tunneling current from the left wide QW to the QD, the p → s radiative transition rate in the QD, and the tunneling current from the QD to the narrow GaAs QW on the right side. The exit current from this QW to the drain is assumed to be infinitely fast. The narrow GaAs QW is designed in such a way that the ground E_1 level is slightly below the E_s level of the QD and that E_2 level is above the E_p level, inhibiting a leakage current from p-level to E_2 level due to energy conservation. There is an optimum energy difference between E_s level and E_1 level to maximize the tunneling current. This energy difference is released into the in-plane kinetic energy of the electrons and the optimum energy requires that the wavelength of the in-plane motion is larger than the dot size.

We have performed numerical computations for the current from a wide QW to the p-level of the QD by 1) computing the p- and s- functions for a designed QD structure, 2) computing self-consistent Hartree wave functions and the energy levels of the wide QW at each field, and 3) computing I-V curve from each QW levels into p-level of the QD and light output.

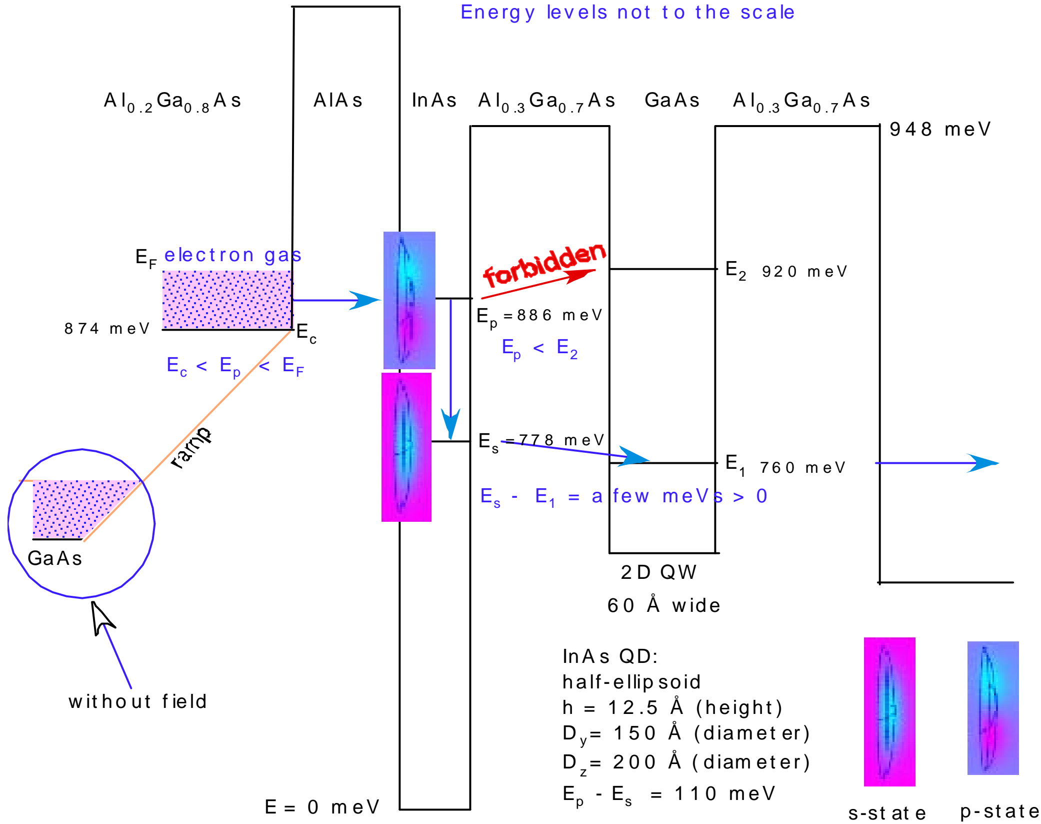

Fig. 2.2: Model structure for tunneling dynamics through InAs quantum dots. The injector stage consists of an electron reservoir. Numerical solutions for InAs quantum dot states are used (and pictured) for calculating tunneling probabilities through the structure. The collector stage consists of a GaAs quantum well specially designed in such a way to enable fast tunneling from the dot ground state, while stifling direct tunneling out of the dot from the upper p-state.

2.2: InAs quantum dot material: growth

It greatly simplifies sample design is the InAs SAQD ground state can be pushed above the GaAs band edge. This leads to easier extraction by GaAs based filter structures. To achieve this arrangement, the InAs dots are grown on AlAs. To meet this end, MOCVD growth of InAs dots on AlAs was developed.

InAs SAQD on AlGaAs nucleates differently than what is observed for InAs SAQD formation on GaAs. The InAs critical layer thickness for SAQD on AlAs is 2.6 Å, larger than the 1.8 Å observed for SAQD formation on GaAs. This is in agreement with

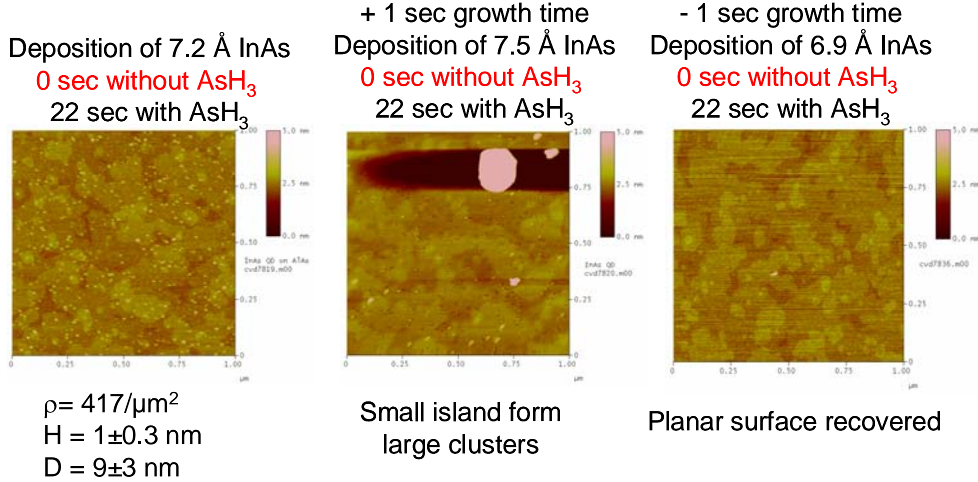

Fig. 2.3: InAs dot nucleation conditions on AlAs using MOCVD. All growths are without the customary precursor starvation used on GaAs. On the left panel, with 7.2A of InAs chemistry, the AFM image shows dot formation. In the center, with only 0.3A more InAs, large cluster form rather than dots. On the right, with only 0.3A less InAs, dot nucleation does not occur. Clearly, the growth conditions for InAs dots on AlAs are very sensitive.

previous studies performed by MBE. We have found that any post-growth purging to remove AsH_3 and metal-organics after InAs deposition is deleterious to the formation of small dense islands. Even a two second purge without AsH_3 leads to ripening, resulting in large 200 nm diameter faceted islands. The density of SAQD increases when higher AsH_3 partial pressures are used for the growth. Photoluminescence from single layer of InAs SAQD grown on AlAs and capped with $Al_{0.3}Ga_{0.7}As$ taken at 77K shows strong emission attributed to SAQD at 1.46 eV, slightly below the GaAs bandedge at 1.49 eV. The dot nucleation behavior and growth conditions are summarized in Fig. 2.3.

2.3: InAs quantum dot material: characterization

As a result of the theoretical efforts and sample design (Fig. 2.2), highlighted in Sec. 2.1, an improved device performance was realized including room temperature elecroluminescence. The emission characteristics of this material are shown in Fig. 2.4. While much work still needs to be done in order to fully realize the potential of InAs dots for mid-IR photonics, this is an exciting results. Previous efforts to achieve mid-IR electroluminsecne, with similar injection/collection schemes, would not operate above 200K. Beyond this, the coupling of the dots to the various device stages was not understood. The imrpoved performance of the sample design of Fig. 2.2 has implications beyond the emission spectra of Fig. 2.4a. The key result here is not that emission was obtained, or that it persisted to elevated temperatures, but that changing the structure surrounding the dot made a difference. Until this work, it was not known, for example, if quantum well filters would work for SAQDs. While it will be some time before SAQD emitters are engineered to the extent of quantum well based QCL systems, these results show that such development is indeed feasible.

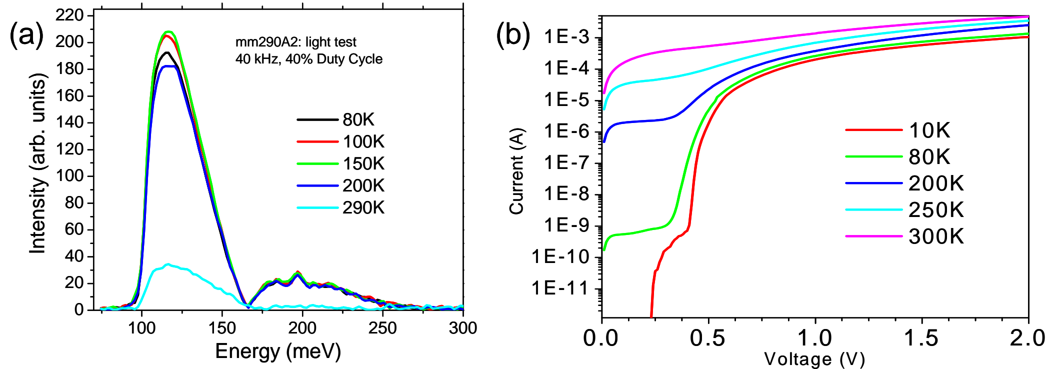

Fig. 2.4: InAs SAQD material characteristics. (a) Electroluminescence spectrum for InAs quantum dot material. Emission persists to room temperature. In (b), temperature dependent IVs are displayed showing a clear 'kink' around 0.4V which corresponds to the injectors state aligning with the upper SAQD states.

2.4: Photonic crystal fabrication

When it comes to photonics, one advantage of working in the mid-IR is that standard optical lithography can be used as opposed to e-beam or more complicated schemes needed for near-IR device. Beyond this, because the InAs SAQD material outlined in this work is a unipolar electron device, it can potentially operate in etched devices where near-IR bipolar (electrons and holes needed) material cannot be electrically pumped due to parasitic recombination at defect sites. While full photonic crystal integration of InAs quantum dot material was not achieved due to limited growth capability, initial steps were taken to demonstrate the in-house capability of making such structures.

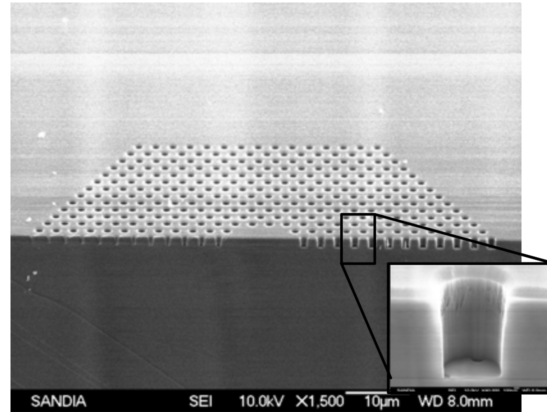

Fig. 2.5: Defect mode photonic crystal cavity test structure made with standard lithography. Inset shows relatively straight sidewall profiles achieved by the plasma etching process.

Figure 2.5 shows an etched photonic crystal test structure that was patterned with standard lithography. The lattice design was for 10μm emission. The etch was performed using standard BCl_3 chemistry in a CAIBE (chemically assisted ion beam etch) system. To fully integrate the InAs SAQD material into this structure would require a new sample design where the dot layer is positioned mid-way through a half wavelength stack. While this is feasible, the growth was not performed to enable the

photonic crystal integration. A final detail about photonic crystal integration is that it necessitates undercutting the lattice in order to create a 2D waveguiding layer. Such undercutting could be possible through the incorporation of an AlAs selective etch layer underneath the active device.

2.5: Mid-IR plasmonics

Although the initial focus of this work was to integrate photonic crystal cavities into InAs quantum dot material, we found that plasmonic couplers could achieve many of the same desired results. Once work had begun along these lines, and we started to learn more about the field, we found that there were many opportunities in the mid-IR to impact the field of plasmonics.

2.5.1: Free-carrier tuning of plasmonic resonances

Metallic films having periodic subwavelength perforations or corrugations have unique transmission properties. Ebbessen et al studied such structures and demonstrated the phenomenon of extraordinary transmission (EOT), where, at certain wavelengths, more light passes through the sample than predicted by aperture theory[2,3]. This effect has been ascribed to surface plasmon (SP) enhancement of the transmission process. There has been significant interest in utilizing such structures for a variety of photonic devices, the majority of which are designed to function in the visible and near-infrared.

Advances in mid-infrared (mid-IR) sources and the growing field of mid-IR photonics make the mid-IR (3 μm - 12 μm wavelength) a very attractive wavelength range into which to extend this technology. Mid-IR SP devices have been shown to have similar properties to structures in the visible[4-6]. Beyond this, it has also been shown that chemical attachment to the mesh surface can enhance the sensitivity of molecular absorption measurements by several orders of magnitude[5].

Here, we experimentally verify a SP resonance tuning mechanism for the mid-IR, free electron tuning of the dielectric constant in a semiconductor. While a related mechanism has been investigated for tuning and switching at terahertz frequencies in pure semiconductor gratings[7], we focus here on metallic gratings fabricated on doped semiconductor substrates using the well studied geometry of a rectangular lattice of holes fabricated in a metal film. A small portion of the grating structure used is shown in the inset of Fig. 2.6. A general expression for the normal incidence SP transmission resonance condition is given by[3]:

$$\sqrt{i^2 + j^2}\,\lambda = a_0\sqrt{\frac{\varepsilon_s \varepsilon_m}{\varepsilon_s + \varepsilon_m}} \approx a_0\sqrt{\varepsilon_s} \;\; for \;\; |\varepsilon_m| >> |\varepsilon_s| \qquad (2.1)$$

Here, λ is the free space wavelength, a_o is the lattice constant, *i* and *j* are integers related to the reciprocal lattice vectors $2\pi/a_o$ **x** and $2\pi/a_o$ **y** respectively, ε_s is the real part of the dielectric constant of the semiconductor (or air) and ε_m is the real part of the dielectric constant of the metal. For commonly used metals (Au, Cu, Ag, Al), in the mid-IR, $|\varepsilon_m|>>|\varepsilon_s|$, so Eq.2.1 reduces to its simpler form.

Equation 2.1 shows that the air/metal and air/dielectric modes will occur at different frequencies due to the differences in dielectric constant between the semiconductor and air. While the details can become quite involved, it has been found that incident light at either set of resonant frequencies, from either side of the metal film, leads to extraordinary transmission[3]. It is not necessary that both surfaces have the same resonant frequency, although that leads to further enhancement of transmission[8,9].

The free electrons in bulk semiconductors can exhibit well known collective charge oscillations, or plasmons, where the natural resonance frequency is given (in CGS units) by $\omega_p^2 = 4\pi n e^2 / \varepsilon m^*$. Here n is the carrier concentration, e is the charge of an electron, ε is the background dielectric constant of the semiconductor, and m^* is the effective electron mass in the semiconductor. Neglecting scattering, the frequency dependent effects of free-carriers can be incorporated into the dielectric function of the semiconductor using[9]

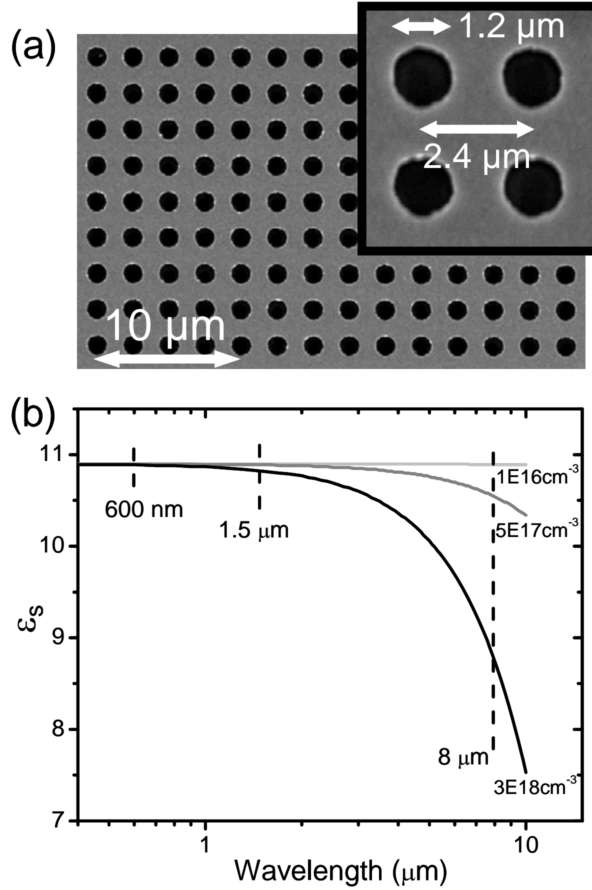

Fig. 2.6: (a) shows scanning electron micrograph of extraordinary transmission grating structure. Part (a) shows the dielectric function of GaAs including the effects of free-carriers. The grating period is 2.4 µm and the individual hole diameters are designed for 1.2 µm. Fabrication widens the actual device hole diameter to ~1.3 µm.

$$\varepsilon(\omega) = \varepsilon\left(1 - \omega_p^2 / \omega^2\right) \tag{2.2}$$

Figure 2.6b displays the frequency dependent dielectric function for various doping concentrations in GaAs. A vertical line in the plot of Fig.2.6b is drawn at wavelengths of 8µm (the design wavelength for the structures studied in this work), 1.5µm (telecom wavelength), and 600 nm (visible). As can be seen, a change in the free carrier concentration of the semiconductor causes a corresponding change in the dielectric constant, which grows increasing pronounced as we move to longer wavelengths. Combining Eq. 2.1,2.2 completes the framework for our SP tuning mechanism.

Three separate samples were studied, 7947, 7952, and 7954. Sample 7952 consists of 2µm of Si-doped GaAs, with a dopant density of $1\cdot10^{16}$ cm^{-3}. Sample 7947 consists of 1.2µm of Si-doped GaAs, doped $5\cdot10^{17}$ cm^{-3}. Finally, Sample 7954 consists of 0.5µm of Si-doped GaAs, doped $3\cdot10^{18}$ cm^{-3}.

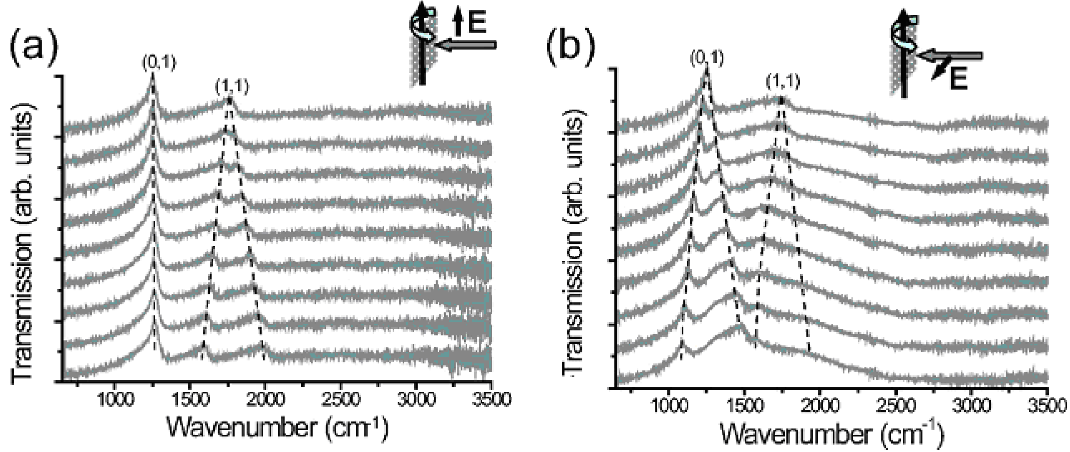

Fig. 2.7: Transmission for highly doped ($3{\cdot}10^{18}cm^{-3}$) sample as a function of incident angle for angles from 0º (top trace) to 32º(bottom trace) in 4º increments. (a) Transmission spectra for light polarized orthogonal to the axis of rotation (b) Transmission spectra for light polarized parallel to the axis of rotation. Dashed lines are added as aids for visualizing the peak splitting in both plots, and follow the peak structure of the spectra. The surface plasmon modes are labeled above the 0º spectra for both (a) and (b). Transmission spectra as a function of incident angle for the more lightly doped samples show identical structure, shifted slightly in wavenumber.

Gratings, consisting of a square lattice of circular openings in a thin metal film, were designed so that the fundamental metal/dielectric mode (i+j=1) would occur at a free-space wavelength of 8 µm on undoped GaAs. This resulted in a design lattice constant of 2.4 µm and hole diameters of 1.2µm, though the final hole diameters achieved were closer to 1.3 µm. The sub-wavelength gratings were fabricated by optical lithography, Ti/Au (100Å/500Å) metallization, and lift-off. Typical peak transmittances for our samples, at 0º incidence angle, are approximately 20% and as large as 27%.

Figure 2.7 shows the transmission spectra for Sample 7954 with light polarized parallel to the axis of rotation (2.7a) and perpendicular to the axis of rotation (2.7b), for incidence angles from 0º to 32º, in 4º steps. The transmission spectra show a clear, polarization-dependent splitting of the SP modes as a function of incidence angle. The angular and polarization dependence of the transmission spectra for our samples are similar to the equivalent measurements of EOT gratings on quartz substrates in the near-IR regime[2].

The position of the fundamental metal/dielectric SP transmission peak is strongly dependent on the dielectric constant of the dielectric material. Figure 2.8 shows the transmission peaks for the three samples considered in this study. Each spectra was taken with incident light polarized as shown in Fig. 2.7a and collimated in order to minimize peak widening due to $k \neq 0$ wavevectors. A clear blueshift of the transmission peak is seen as the doping level of the semiconductor substrate is increased. A shift of ~$23cm^{-1}$ is seen when the sample 7952 (doping of $1{\cdot}10^{16}$ cm^{-3}) is compared to sample 7954 (doping of $3{\cdot}10^{18}$ cm^{-3}). It should be noted, however, that the magnitude of the transmission peak shift is less than was calculated using Eq. 2.1,2.2. This may be a result of a number of factors, including the varying thicknesses of the doped epilayers and surface depletion effects at the metal/dielectric interface.

The width of the transmission peak will be determined by a number of factors, such as inhomogeneity in the dielectric, nonuniformity of the grating, and the range of wavevectors incident on the grating. The wavevector broadening comes from the fact that SPs have a dispersion with respect to in plane wavevector[3]. To determine the width of the transmission peak in our grating samples, we studied the spectral characteristics of the first order SP transmission mode as a function of the entrance optics used to couple light into the gratings. The results are shown in the inset to Fig. 2.8. As the focal length of the entrance optics is increased (from 2" to 6" to ∞, or collimated light), we see a distinct narrowing of the transmission peak. As longer focal lengths are used, the range of k-vectors incident on the grating surface narrows as the in-plane k components are reduced. For collimated light, we see a peak width of 18cm^{-1} (~2.2meV), over a fourfold improvement from the 2" entrance optics, which give a broadening of 86cm^{-1}.

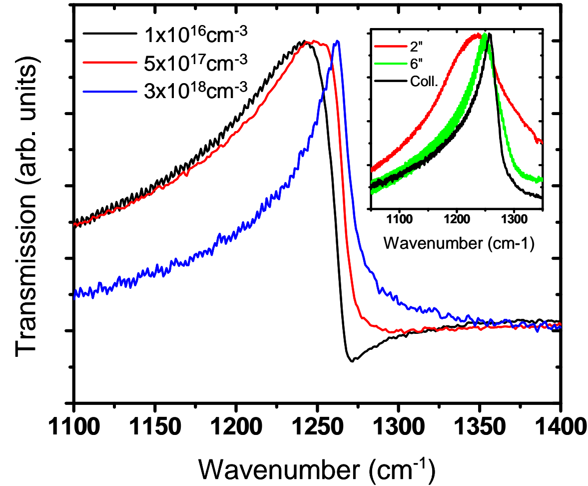

Fig. 2.8: Polarized transmission spectra for all three samples at 0° incident angle, focusing on the fundamental peak. The transmission peaks show a distinct shift as the doping of the epitaxial layer is increased. The transmission peak positions for each sample are: 7954 (doped $3\cdot10^{18}$cm^{-3}): 1263cm^{-1}; 7947 (doped $5\cdot10^{17}$cm^{-3}): 1248cm^{-1}; 7952 (doped $1\cdot10^{16}$cm^{-3}): 1240cm^{-1}. The inset shows the peak structure for sample 7954 as a function of the focusing optics used (using unpolarized light). As the focal length of the lens increases, from 2" to ∞ (collimated light), the width of the transmission peak decrease from 86cm^{-1} to 18cm^{-1}.

2.5.2: Temperature tuning of plasmonic resonances

As noted in Sec. 2.5.1, perforated metal films can exhibit extraordinary optical transmission (EOT) where, at certain wavelengths, more light passes through the sample than predicted by aperture theory[1]. While current work with passive EOT structures has shown great promise, the ability to electrically tune such devices would add greater functionality to a variety of photonic applications. In Sec. 2.5.1, we have shown that changing the carrier concentration in GaAs epilayers can shift the transmission peak of mid-IR EOT structures[11]. For n-type doping densities varying from 1 x 10^{16} cm^{-3} to 3 x 10^{18} cm^{-3} a shift of 0.14μm (22 cm^{-1}) was achieved for gratings transmitting at 8μm (1250cm^{-1}). While that work achieved EOT peak shifts utilizing separate samples, we show in this letter that even greater shifts can be achieved from a single device using electronically controlled current tuning of the EOT structure.

The sample studied, shown in Fig. 2.9a,b, was grown by metal-organic chemical vapor deposition and consists of a 100nm thick n-doped (3.5x10^{18} cm^{-3}) GaAs epilayer above an undoped 50nm $Al_{0.2}Ga_{0.8}As$ epilayer and an undoped GaAs buffer layer on a

semi-insulating GaAs substrate. Fabrication of the device consisted of a mesa etch through the doped epilayer, followed by evaporation and annealing of ohmic (235A Ge/470A Au/300A Ni/1000A Au) source and drain contacts. A 10nm/50nm Ti/Au square lattice grating (2.8µm period, 1.5µm holes) was then defined using optical photolithography and a lift-off metallization process. Light transmission through such a structure relies on SP excitations at the air/metal and the metal/dielectric interfaces. A general expression for the normal incidence SP resonance condition is given by[3]:

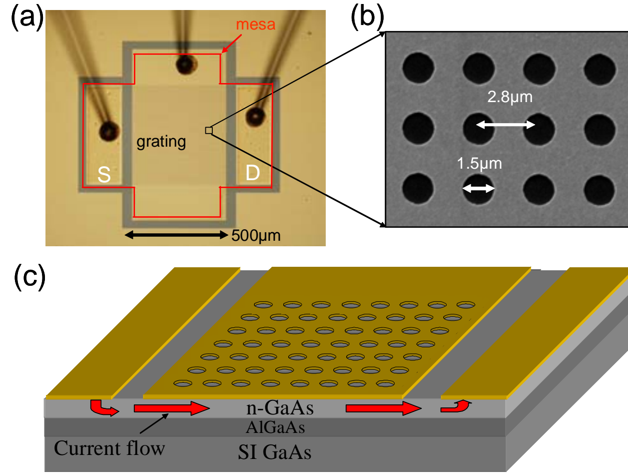

Fig 2.9: Tunable mid-infrared extraordinary transmission device. (a) Optical micrograph of tunable EOT device with labeled Source contact (S), Drain contact (D), and grating. (b) Scanning electron micrograph of transmission grating designed for transmission at 9um. (c) Schematic of tunable EOT device showing current path through n-doped GaAs epilayer, source and drain contacts and transmission grating (not to scale).

$$\sqrt{i^2+j^2}\,\lambda = a_0\sqrt{\frac{\varepsilon_s\varepsilon_m}{\varepsilon_s+\varepsilon_m}} \approx a_0\sqrt{\varepsilon_s}\ \ for\ |\varepsilon_m| >> |\varepsilon_s| \quad (2.3)$$

Here, λ is the free space wavelength, a_o is the lattice constant (2. 8µm), *i* and *j* are integers related to the reciprocal lattice vectors $2\pi/a_o$ **x** and $2\pi/a_o$ **y** respectively, ε_s is the real part of the semiconductor(air) dielectric constant and ε_m is the real part of the dielectric constant of the metal. For Ti/Au, in the mid-IR, $|\varepsilon_m|>>|\varepsilon_s|$, so Eq.2.3 reduces to its simpler form in this case. The spectral position of the transmission peak related to the metal/semiconductor SP can be tuned by varying a_o or ε_s. When current is passed under the metal mesh, as shown in Fig.2.9c, the epilayer is resistively heated, tuning both of these parameters, to varying degrees, simultaneously.

The normalized mid-IR transmission for our device as a function of electrical current is displayed in Fig. 2.10. Current was applied between the source and drain contacts using a DC power supply operating in constant current mode. Data collection was initiated upon stabilization of the Source-Drain voltage. The transmission spectra exhibit the Fano-lineshape associated with EOT structures[12]. A transmission peak redshift of approximately 25 cm^{-1} is achieved as the source-drain current is tuned from 0 to 200mA (0 to 1.86W power dissipated). The strength of the transmission peak does not decrease substantially (~25% reduction) at the highest current. Additionally, we see no increase in the peak linewidth as a function of current. Both of these results suggest that scattering and free carrier losses do not significantly affect device performance at high temperatures. The tuning achievable with such a configuration, in addition to the stable transmission strength and linewidth, suggest that such devices could be utilized as actively tunable mid-IR optical components.

Many physical changes are associated with temperature changes that can cause the observed shift. To accurately model these, the temperature of the device as function of

current must be determined. Temperature calibration was obtained by band edge photoluminescence (PL) spectroscopy. As the current is increased and the sample is heated, the semiconductor band edge shifts as shown in the inset of Fig. 3. By tracing the position of the GaAs band edge PL as a function of current, an approximate value for the device temperature is found using the empirical relation for the temperature (K) dependence of the GaAs band gap (eV)[13].

$$E_G(T) = 1.519 - 5.405x10^{-4} T^2 /(T + 204) \quad (2.4)$$

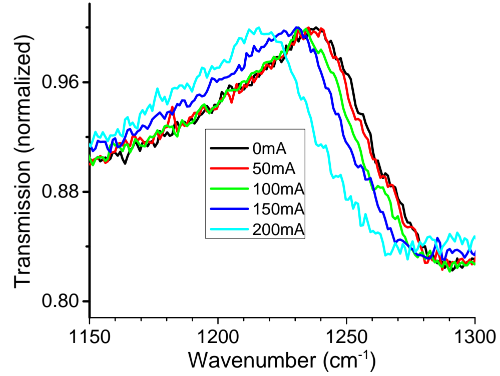

Fig. 2.10: Transmission spectra at various currents. Normalized transmission spectra for 8μm tunable surface plasmon device as a function of source-drain current. A clear redshift can be seen as the current is increased from 0 to 200mA. The maximum shift achieved was 25cm^{-1}.

As shown in Fig. 2.11, the temperature of the device can be tuned from 300K (0mA) to over 550K (200mA). From a geometrical standpoint, thermal expansion can change a_o which, according to Eq. 2.3 would lead to a redshift in the SP transmission peak. This is only a small effect (~2cm^{-1}) at the highest temperatures. In our semiconductor medium, there are several competing temperature dependent dielectric shifts. In the undoped material, we must consider the thermal generation of free carriers and the temperature dependence of the dielectric constant. In the relatively thin doped layer, which contains a high density of built-in free carriers, these effects must be considered along with the reduction of both the semiconductor plasmon damping time and in the free carrier effective mass. The thin $Al_{0.2}Ga_{0.8}As$ layer, having optical properties very similar to GaAs[14] (and because it is very thin compared to the wavelengths of interest) is modeled together with the undoped GaAs buffer layer for simplification.

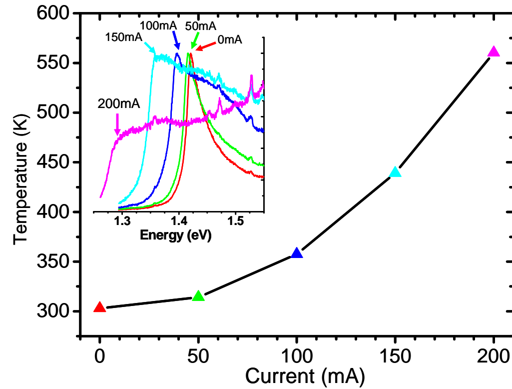

Fig. 2.11: Device surface temperature derived from photoluminescence spectra (inset) as a function of current. For a fixed current, photoluminescence was used to relate the position of the GaAs band-edge to the device temperature. The main plot shows the resulting temperature calibration.

The temperature dependence of the semiconductor dielectric function can be modeled using the Drude approximation, including scattering, as:

$$\varepsilon(\omega,T,n) = \varepsilon_b(T)\left(1 - \frac{\omega_p(T,n)^2}{\omega^2 + i\omega\gamma(T,n)}\right), \quad \omega_p(T,n)^2 = \frac{4\pi n(T)e^2}{\varepsilon_b(T)m^*(T,n)} \quad (2.5)$$

Here, $\omega_p(T, n)$ is the plasma frequency, $\gamma(T, n)$ is the plasmon damping term ($=1/\tau$ where τ is the scattering time), $n(T)$ is the carrier concentration, e is the charge of an

electron, $\varepsilon_b(T)$ is the background high frequency dielectric constant of the semiconductor, and $m^*(T, n)$ is the effective electron mass in the semiconductor. The shift of the SP resonance is modeled using the temperature and doping dependent relationships for the above parameters (m^*, ω_p, γ, n, ε_b)[13,15] and the results are displayed in Fig. 2.12a. The modeled shift is greatest for the undoped GaAs buffer and substrate, and is explained by the temperature dependence of the GaAs dielectric constant[13]:

$$\varepsilon_b(T) = 10.6(1 + T \cdot 9 \times 10^{-5}) \qquad (2.6)$$

Thermal generation of carriers can only create bulk densities on the order of $1\text{x}10^{13}\text{cm}^{-3}$ at our elevated temperatures, which is orders of magnitude too low to provide any noticeable shifting of the SP peak. The additional temperature dependent terms in Eq. 2.5 do, however, affect the peak position expected at higher temperatures for doped material. In Fig. 2.12a, as the doping of the semiconductor is increased, the redshift of the transmission peak is somewhat offset by the Drude contribution to the dielectric function.

Figure 2.12b shows the calculated redshift for an 8µm grating device (black dashed) assuming an undoped GaAs dielectric along with the measured peak positions (red). Since the redshift in our devices is greater than that predicted by temperature tuning of the undoped dielectric, it is argued that the majority of the metal/semiconductor SP field lies in the undoped material, and the thin, highly doped GaAs layer serves mostly as a heating mechanism with minimal influence over the SP transmission peak spectral position.

A decrease in transmission peak strength of ~25% is seen as the device temperature is increased. This is most likely due to increased losses in both the 500µm GaAs substrate and at the interface between the metal mesh and the highly doped GaAs epilayer.

2.5.3: Active Control of Propagating Surface Plasmons

Here we investigate the coupling between an array of subwavelength apertures in a metal film and a dual wavelength Quantum Cascade Laser. We demonstrate that by actively tuning the optical properties, as in Sec. 2.5.2, of our plasmonic surface and measuring its spectral and spatial transmission, we are able isolate the resonant transmission and propagating surface wave phenomena on the plasmonic surface. The ability to control the launching of long-range surface plasmons (~400µm) was

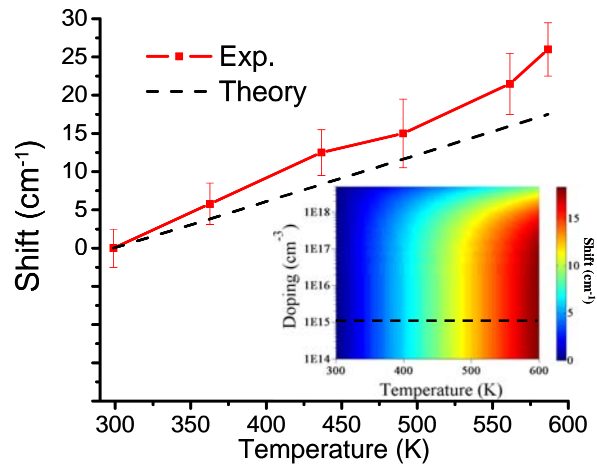

Figure 2.12: Calculated and experimental redshift of tunable SP grating devices as a function of temperature. (inset) The calculated magnitude of the spectral shift as a function of both doping and temperature. As the doping is increased, less of a redshift is expected. The calculated (black dashed) and experimental (red solid) redshifts.

demonstrated.

The dispersion relation for surface plasmon excitations can be found by solving Maxwell's Equations for surface propagating waves, using the appropriate boundary conditions. The resulting expression gives the SP wavevector as a function of the excitation frequency ω (Eq 2.7a), where k_{sp} is the SP wavevector and ε_s and ε_m are the relative permittivities of the dielectric material and the metal, respectively.

$$(a) \quad k_{sp} = \frac{\omega}{c}\sqrt{\frac{\varepsilon_s \varepsilon_m}{\varepsilon_s + \varepsilon_m}} \qquad (b) \quad k_{sp} = k_{xphoton} \pm \frac{2\pi}{a_o} m \quad , \quad k_{xphoton} = k_{photon} \sin\theta \qquad (2.7)$$

In order to couple a free space photon into such a mode, momentum must be conserved. For periodically modulated metal films, this is achieved by means of a grating wavevector associated with the periodicity of the film. The resulting momentum conservation expression, for a SP propagating in the x-direction only, can be written as shown in Eq.2.7(b), where a_o is the periodicity of the metal film, $k_{xphoton}$ is the in-plane momentum component of the photon incident at an angle θ, and *m* is an integer. At normal incidence, for light polarized in the x-direction, the forward (1,0) and backward (-1,0) propagating modes are degenerate. However, for θ≠0, these two SP modes split, which is evidenced by a splitting of the primary peak in the extraordinary optical transmission (EOT) grating transmission spectra[3]. Thus, photons resonant with the lower frequency (ν-) peak should couple to SPs propagating in the –x direction, while those resonant with the higher frequency (ν+) transmission peak would be expected to couple to SPs propagating in the +x direction.

The EOT grating used here had a peak transmission at ~9.5μm. We use a dual wavelength liquid nitrogen-cooled, pulsed quantum cascade laser (QCL), emitting at ~5.6 and ~9.7 μm, as the incident light source for this work. Figure 2.13 depicts both the QCL emission spectrum and the normal incidence EOT mesh transmission spectrum for the laser and grating used in this work.

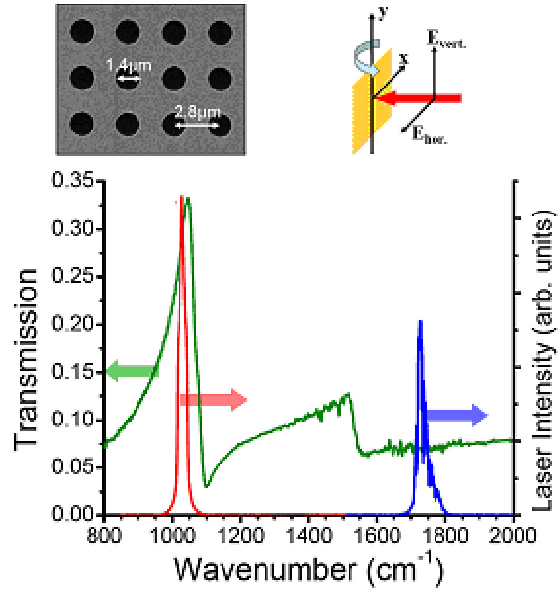

Fig. 2.13: Dual wavelength QCL emission spectrum and normal incidence, room temperature broadband transmission through EOT grating sample (green). Insets show, from left to right, scanning electron micrograph of EOT grating surface, and diagram of coordinate system used in this work.

Spectral characterization of the EOT grating was performed using a Bruker V70 Fourier Transform Infrared (FTIR) spectrometer. A broadband mid-IR source was focused on the grating through a wire-grid polarizer passing only horizontal (x) polarized light, and transmission spectra were collected as a function of sample rotation around the vertical (y) axis, as depicted in Figure 2.14. A clear splitting of the primary transmission peak is seen (Figs 2.14a and 2.14c), corresponding to lifted

degeneracy of the (1,0) and (-1,0) SP modes resulting from the non-zero in-plane incident photon momentum. Active control of the plasmonic resonance was achieved via thermal tuning of the GaAs substrate. As shown in Figure 2.14b, the thermal tuning of the grating results in a redshift of the transmission peak of approximately 20 cm^{-1}.

Control of SP propagation on the plasmonic surface should be observed when a resonant frequency of the EOT grating can be tuned on and off the QCL laser line. Using the grating transmission and tuning properties determined by broadband transmission experiments, it was determined that an incidence angle of 8º would position the 9.7 μm QCL line on the (-1,0) room temperature EOT transmission peak (Fig. 2.14a). Upon tuning, as shown in Fig. 2.14c, this QCL line would move to sit on the high energy side of the peak, off of the transmission peak associated with the (-1,0) SP mode.

The 9.7 μm light is focused onto the EOT surface to a spot size of ~50μm and transmitted/scattered light as a function of frequency and x-position is measured across the sample surface. At room temperature, when the long wavelength laser is spectrally aligned with the (-1,0) transmission peak, no propagation is seen on the sample surface. However, as the EOT grating is redshifted through temperature tuning, the laser line now lies upon the high energy side of the (-1,0) peak and a distinct propagation of the incident light is seen, evidenced by the transmitted/scattered intensity tail extending in the –x direction from the laser spot shown in Fig. 2.15a. No propagation is seen for vertically polarized light, as expected.

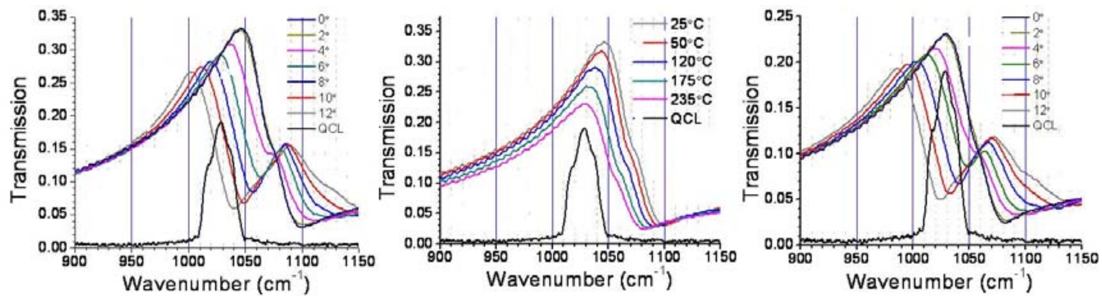

Fig. 2.14: Long wavelength QCL spectra and EOT spectra. (a) room temperature EOT transmission spectra for incidence angles from 0-12º, (b) normal incidence EOT transmission spectra for temperatures from 25 to 235ºC, and (c) Shifted, 235ºC EOT transmission spectra for incidence angles

From the data in Figure 2.15, we can estimate a decay length for the propagating excitation[16] of approximately 384 µm. The calculated propagation length for a SP, at this wavelength and temperature, using the theory in ref. 16, is 945µm for Au. Though our results show a somewhat shorter propagation length, it must be noted that our sample is not a pure Au, but has a thin Ti layer between the Au and the substrate, for adhesion purposes. The calculated length also is for an un-modulated metal-GaAs surface, whereas our experiment uses a surface with periodic apertures in the metal.

The above results indicate that we are able to excite the propagating mode on the sample surface by active control of the EOT grating's optical properties. By incorporating the free-carrier tuning of Sec. 2.5.1 into a similar scheme, one can envision voltage controlled transistor like structures that, when operating under proper conidtions, can control light on chip.

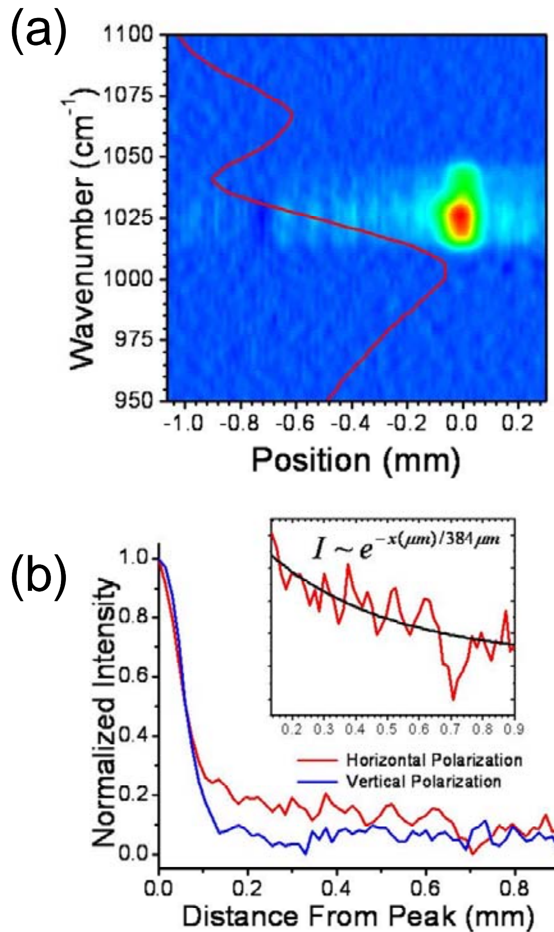

Fig. 2.15: Controlled excitation of the surface plasmon. In (a) the bright spot positioned at 0mm is the focused laser. When tuned to the falling edge of the EOT transmission structure, a SP wave launched in the –x direction was observed. Part (b) pictures an intensity plot over this region for both horizontal and vertical polarization. Clearly, the verticle polarization does not behave in the same way. A decay length of 384µm was measured.

3. CONCLUSIONS

The work performed under this project opens some exciting paths towards future opportunities. In terms of mid-IR emitters, the potential to make quantum cascade laser structures using quantum dots instead of quantum wells is exciting. While developing that field will take a significant amount of time and resources, it could have a potentially high payoff in terms of increasing QCL wall-plug efficiency. On the photonics side, while photonic crystal cavity integration will happen eventually, and likely produce interesting results, at this stage, it is more important to focus on material issues. The surface plasmon aspects of this work were somewhat of an offshoot to the primary original goals of this project, however, our measurements show an example of how one technology or research area can spin off and leads to results impacting another. Our work performed in that area provide the basic building blocks for photonic transistors (where light carries information as opposed to electrons), as well as some plasmon tuning concepts that will be applied to mid-IR beam-steering and other novel device concepts.

4. REFERENCES

1. O. Stier, et. al., PRB 1999, 59, 5688
2. T. W. Ebbesen, H. J. Lezec, H. F. Ghaemi, T. Thio, and P. A. Wolff, Nature 391, 667 (1998).
3. H. F. Ghaemi, T. Thio, D. E. Grupp, T. W. Ebbesen, and H. J. Lezec, Phys. Rev. B 58 (11) (1998).
4. Y.H. Ye and J. Y. Zhang, Appl. Phys. Lett. 84 (16) (2004).
5. K.R. Rodriguez, S. Shah, S. M. Williams, S. Teeters-Kennedy, and J. V. Coe, J. Chem. Phys. 121 (18) (2004).
6. S.M. Williams, A. D. Stafford, T. M. Rogers, S. R. Bishop, and J. V. Coe, Appl. Phys. Lett. 85 (9) (2004).
7. C. Janke, J. G. Rivas, P. H. Bolivar, and H. Kurz, Opt. Lett. 30 (18) (2005).
8. A. Krishnan, T. Thio, T. J. Kima, H. J. Lezec, T. W. Ebbesen, P. A. Wolff, J. Pendry, L. Martin-Moreno, and F. J. Garcia-Vidal, Opt. Commun. 200 (1-6) (2001).
9. L. Martin-Moreno, F. J. Garcia-Vidal, H. J. Lezec, K. M. Pellerin, T. Thio, J. B. Pendry, and T. W. Ebbesen, Phys. Rev. Lett. 86 (6) (2001).
10. C. Kittel, Introduction to solid state physics, 7th edition. (John Wiley & Sons, Inc., New York, 1995).
11. D. Wasserman, E. A. Shaner, and J. G. Cederberg, Appl. Phys. Lett. 90, 191102 (2007).
12. L. Pang, K. A. Tetz, and Y. Fainman, Appl. Phys. Lett. 90, 111103 (2007).
13. J. S. Blakemore, J. Appl. Phys. 53, R123 (1982).
14. S. Gehrsitz, F. K. Reinhart, C. Gourgon, N. Herres, A. Vonlanthen, and H. Sigg, J. Appl. Phys. 87, 7825 (2000).
15. K. H. Nichols, C. M. L. Yee, and C. M. Wolfe, Solid-State Electron. 23, 109 (1980).
16. W.L. Barnes, "Surface plasmon-polariton length scales: a route to sub-wavelength optics", J. Opt., 8, S87 (2006).

APPENDIX A: METRICS

- Publications
  - E. A. Shaner, J. G. Cederberg, and D. Wasserman, Appl. Phys. Lett. 91, *Electrically tunable extraordinary optical transmission gratings*, 181110 (2007)
  - D. Wasserman, E. A. Shaner, and J. G. Cederberg, *Midinfrared doping-tunable extraordinary transmission from sub-wavelength gratings*, Appl. Phys. Lett. 90, 191102 (2007)
  - D. Wasserman, C. Gmachl, S. A. Lyon, and E. A. Shaner, *Multiple wavelength anisotropically polarized mid-infrared emission from InAs quantum dots*, Appl. Phys. Lett. 88, 191118 (2006)
- Proceedings
  - D. Wasserman, S. H. Howard, C. Gmachl, S. A. Lyon, J. Cederberg, and E. A. Shaner, *Mid-infrared electroluminescence from InAs self-assembled quantum dots*, Proc. SPIE 6386, 63860E (2006)
- Patents
  - "Tunable Surface Plasmon Devices" applied for in June, 2008
- Active Collaborations:
  - Dan Wasserman (UMass Lowell)

Distribution

1	MS0123	D. Chavez, LDRD Office	1011
1	MS1082	Ihab El-kady	1725
1	MS1082	J.J. Hudgens	1725
1	MS1082	Ganesh Subramania	1725
1	MS1086	Dan Barton	1123
1	MS1086	Bob Biefeld	1126
1	MS1086	Jeff Cederberg	1126
1	MS1415	E.A. Shaner	1123
1	MS1415	S.K. Lyo	1123
1	MS1421	J.A. Simmons	1120
1	MS1427	J.M. Phillips	1100
1	MS0899	Technical Library	9536 (electronic copy)

Sandia National Laboratories